Kinetic, Structural, and Spectroscopic Identification of Geminate States of Myoglobin: A Ligand Binding Site on the Reaction Pathway†

L. Powers,‡ B. Chance,*,§ M. Chance,§ B. Campbell,‡ J. Friedman,‡ S. Khalid,§ C. Kumar,∥ A. Naqui,§ K. S. Reddy,§ and Y. Zhou§

AT&T Bell Laboratories, Murray Hill, New Jersey 07974, Department of Biochemistry and Biophysics, University of Pennsylvania, and Institute for Structural and Functional Studies, Philadelphia, Pennsylvania 19104, and School of Life Sciences, Northeastern Hill University, Shillong 793 014, India

Received August 5, 1986; Revised Manuscript Received February 11, 1987

ABSTRACT: Elementary steps or geminate states in the reaction of gaseous ligands with transport proteins delineate the trajectory of the ligand and its rebinding to the heme. By use of kinetic studies of the 765-nm optical "conformation" band, three geminate states were identified for temperatures less than ~100 K. Mb*CO, which is accumulated by photolysis between 1.2 and ~10 K, was characterized by our previous optical and X-ray absorption studies [Chance, B., Fischetti, R., & Powers, L. (1983) *Biochemistry 22*, 3820–3829]. Between 10 and ~100 K, geminate states are also identified that have recombination rates of $\sim 10^3$ s^{-1} and $\sim 10^{-5}$ s^{-1} (40 K). Thus, it is possible to maintain a steady-state nearly homogeneous population of the slowest recombining geminate state, Mb**, by regulated continuous illumination (optical pumping). Both X-ray absorption and resonance Raman studies under similar conditions of optical pumping show that the heme structure around the iron in Mb** is similar to that of Mb*CO. In both geminate states, the iron–proximal histidine distance remains unchanged (±0.02 Å) from that of MbCO while the iron to pyrrole nitrogen average distance has not fully relaxed to that of the deoxy state. In Mb*CO the CO remains close to iron but not bound, and the Fe···CO angle, which is bent in MbCO (127 ± 4°C), is decreased by ~15° [Powers, L., Sessler, J. L., Woolery, G. L., & Chance, B. (1984) *Biochemistry 23*, 5519–5523]. The CO molecule in Mb**, however, has moved approximately 0.7 Å further from iron. Computer graphics modeling of the crystal structure of MbCO places the CO in a crevice in the heme pocket that is just large enough for the CO molecule end-on. Above approximately 100 K resonance Raman studies show that this structure relaxes to the deoxy state.

The search for and the characterization of intermediate states in the process of ligand binding to proteins are now the principal focus of a variety of studies since the static structures, prior and subsequent to ligand binding, have been well characterized. Kinetic studies are appropriate for identifying the time and temperature domains in which intermediate states can be isolated. The carbonyl, nitrosyl, and oxygen compounds of heme proteins have provided model systems for such studies (Austin et al., 1973; Iizuka et al., 1974a). The Yonetani group showed that the CO photoproducts of hemoglobin and myoglobin (Mb) at low temperatures have near-infrared absorption spectra shifted from the deoxy species (Iizuka et al., 1974b; Yonetani et al., 1973). Subsequently, Frauenfelder and colleagues observed power law kinetics for the recombination reaction on time scales from 10^{-5} to 1.0 s (Ansari et al., 1985; Austin et al., 1975; Frauenfelder, 1985). These results demonstrate the complexity of single-flash myoglobin kinetics and provide evidence for many possible intermediate states.

Optical pumping, which employs regulated continuous illumination at a constant temperature, allows for the possibility of numerous photolysis turnovers producing steady-state concentrations of intermediate states (Chance, B., et al., 1986). Specific intermediates isolated in steady-state concentrations depend only on the respective rates of recombination and the constant temperature illumination intensity: very labile states turn over rapidly and contribute negligibly to the steady-state populations. Using continuous illumination for various times and temperatures, we observe three intermediate states upon MbCO photolysis. At 40 K, a state with a recombination rate constant of 2×10^{-3}/s is distinguishable from two slower states, both with rate constants of $\sim 10^{-5}$/s but differing by a factor of 3.[1]

The purpose of this study is to further characterize the properties of these distinct kinetic populations of photodissociated MbCO. X-ray absorption and resonance Raman spectroscopy are used to elucidate the structure of the heme and its environment whereas optical studies are used primarily for the kinetic assignments. The major focus of our attention, with respect to structure, is the influence and the role of the distal and proximal environments about the iron in determining the kinetically distinct species. The slower kinetic populations are designated, in order of increased recombination time, Mb* and Mb**.

Mb*CO studied by the Yonetani group has been the focus of resonance Raman (Rousseau & Argade, 1986), Mössbauer (Spartalian et al., 1976), IR (Alben et al., 1982), and extended X-ray absorption fine structure (EXAFS) spectroscopies

† This work was supported in part by NIH Grants HL-18708, GM-33165, RR-01633, and GM-31992 and by SSRL Project 107B, supported by NSF through the Division of Materials Research and the NIH through the Biotechnology Resource Program in the Division of Research Resources in cooperation with the Department of Energy.

* Author to whom correspondence should be addressed.

‡ AT&T Bell Laboratories.

§ University of Pennsylvania and Institute for Structural and Functional Studies.

∥ Northeastern Hill University.

[1] The terms "states" and "populations" are used interchangeably here to describe molecules having similar kinetic, spectroscopic, and structural properties which are isolated by optical pumping.

0006-2960/87/0426-4785$01.50/0

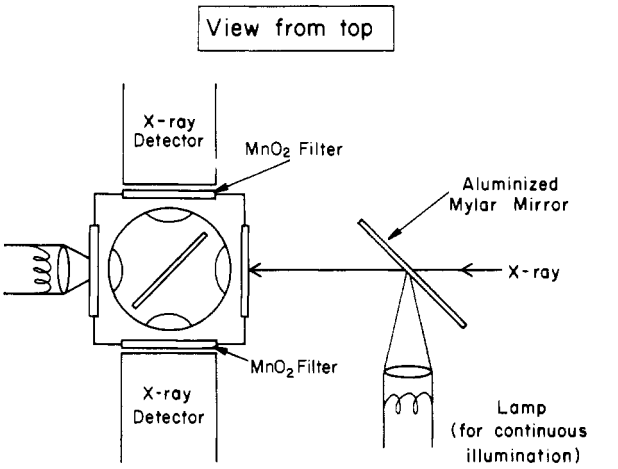

FIGURE 1: Configuration for the acquisition of X-ray absorption spectroscopy data with continuous optical pumping and X-ray detection on both sides of the sample. The aluminized mylar window transmits the X-ray beam. In this case, the spectroscopic measurement is not made simultaneously but is made by trapping the geminate state at 4 K and recording the optical spectrum with the pump light off as described in the text.

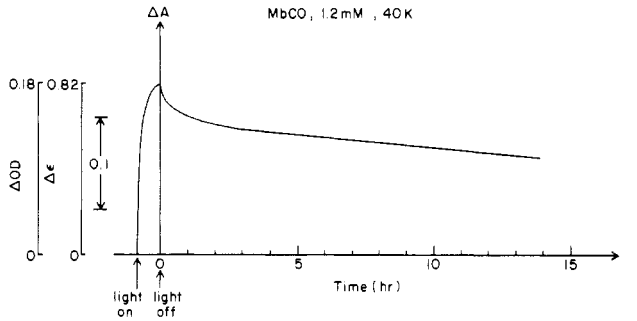

FIGURE 2: Typical protocol for the optical pumping of an MbCO sample (1.2 mM) at 25 and 40 K (see also Figure 4). The wavelength employed here is 764 nm (1.2 mM MbCO, Wratten 88A, and Corning 4010), as in Figure 1 of Chance et al. (1983).

(Chance et al., 1983) as well as magnetic susceptibility measurements (Roder et al., 1984). Mb*CO is trapped by illumination of MbCO at very low temperature (<10 K) and has an absorption band at 765 nm[2] (Ansari et al., 1985; Iizuka et al., 1974b; Chance et al., 1983). The corresponding deoxy-Mb peak is at 758 nm whereas MbCO is essentially silent in this spectral region. The EXAFS results for Mb*CO (Chance et al., 1983; Powers et al., 1984) indicate a heme structure that is different from deoxy-Mb with respect to those parameters to which it is sensitive, i.e.,first coordination shell bond distances. The Fe–proximal histidine distance resembles that of the liganded state, implying that the histidine has not relaxed. Also, the CO has not moved significantly away from the heme, but the change in angle suggests, in accordance with the optical spectrum, that it is no longer bonded to iron. The iron–pyrrole nitrogen distances are intermediate between deoxy and liganded, slightly closer to the deoxy value. Resonance Raman spectra in the "core" sensitive regions of Mb*CO show the "core" to be more expanded than in deoxy-Mb (Rousseau & Argade, 1986), with the suggestion that the iron is not fully out of the heme plane, possibly reducing the iron–pyrrole nitrogen distance relative to deoxy as seen in the EXAFS (Chance et al., 1983). In fact, ligand field indicator region (LFIR) of the X-ray absorption spectrum (Chance et al., 1983, 1984; Chance, B., et al., 1986) shows iron to be 0.35 ± 0.07 Å out of the heme plane, ~0.1 Å less than deoxy-Mb (Chance, 1986).[3] Mössbauer data (Spartalian et al., 1976; Marcolin et al., 1979) and magnetic susceptibility measurements (Roder et al., 1984) provide direct evidence of the high-spin ($S = 2$) nature of Mb*CO, confirming the bond-breaking process. The spectra show differences between deoxy-Mb and Mb*CO that are clear and reproducible but structurally uninterpretable. IR spectroscopy (Alben et al., 1982) shows that the CO stretching frequencies of the photoproducts observed at low temperatures are nearly that of the free gas. In addition, relative changes in the IR intensity of bands associated with photolyzed CO species have been observed with changes in temperature. This is quite compatible with the EXAFS result, which indicates that the CO can be close to the iron but not bonded (Chance et al., 1983; Powers et al., 1984).

Optical studies presented here of the kinetics of the 765-nm band also demonstrate different species above 10 K. Both the EXAFS and Raman results indicate that the structure of the heme and proximal histidine change very little in going from Mb*CO to Mb**; the largest change is for the ligand that EXAFS results show has moved ~0.7 Å further away. This

[2] This band was originally observed at 772 nm, but more recent studies locate it at 764–766 nm (Ansari et al., 1985; Iizuka et al., 1974b; Chance et al., 1983).

[3] It should be noted here that the position of the CO in Mb*CO relative to the heme is identical with that of O_2 in MbO_2. X-ray absorption studies of MbO_2 at 4 K (Powers et al., 1984; Chance, M., et al., 1986) agree with the high-resolution crystallography results of Phillips (1980) that the Fe–O–O angle is 115°, Fe–O = 1.83 Å, and the Fe is out of the plane ~0.2 Å. In Mb*CO, the Fe···C–O angle is 117 ± 4°, and Fe–C = 1.97 ± 0.2 Å, but the Fe is ~0.35 Å out of the heme plane. This places the CO in the same position as O_2 with respect to the heme, and thus, the van der Waals repulsive forces from the heme are not unusual but comparable to those in MbO_2. On the other hand, the O_2 is bound at a normal distance and angle for bonding of its π orbitals while the distance and angle are highly unusual for π bonding of the σ orbital of CO. In addition, the Fe–N_p average distance in Mb*CO is increased relative to MbCO with the Fe out of the plane, and this is consistent with the CO not bound, as the result of other investigations demonstrate. The reason the CO remains close but not bound to the iron in this 4 K photoproduct is speculative, but several results are relevant. Steric factors from the pocket architecture influence the Fe–C–O angle and Fe–C bond distance (Powers et al., 1984) as well as the CO and O_2 binding properties in model compounds (Collman et al., 1983). The Fe–C–O angle in MbCO is significantly bent (Norvell et al., 1975; Powers et al., 1984; Kuriyan et al., 1986) from the linear CO position normal to the heme as found in open-cavity model compounds, and the Fe–C distance is ~0.15 Å longer. This angle and bond distance of myoglobin, together with the CO and O_2 association and dissociation rates, are similar to the distal side steric encumbered "pocket model" (Collman et al., 1983) and suggest that the pocket architecture plays a role in the position of the CO. The CO is not H-bonded to the distal histidine as is O_2 (Norvell et al., 1975), but the CO is in similar proximity to both the heme and distal histidine (Kuriyan et al., 1986) which may represent a local energy minimum. Although the kinetic energy imparted to the CO on photolysis is not known, there are many mechanisms available to the heme for dissipation of this absorbed energy, and the action spectrum at 4 K (Chance et al., 1983) shows that photons having wavelengths extending into the infrared minor heme absorptions may be effective in the photolysis of MbCO. The repulsive van der Waals force that results from the $3d_{z^2}$ orbital of the iron heme and the σ orbital of the photolyzed CO is difficult to evaluate. The electron probability distribution density (shape of the orbital) for the $3d_{z^2}$ orbital of Ti(III) is reduced to only 10% of its maximum at ~0.9 Å in the z direction, reaching a maximum width of ~0.6 Å at ~0.6 Å (z direction) on this constant electron density contour, while the $2p_z$ orbital of C is reduced to this value at ~1.0 Å, reaching a maximum width of ~1.4 Å at ~0.6 Å (Ogryzlo & Porter, 1963). Although the $3d_{z^2}$ orbital of Fe(II) is similar to that of Ti(III), it is reduced by the heme and proximal histidine and the $2p_z$ is reduced by the triple bond to O. The decrease of the Fe···C–O angle in Mb*CO would further lower the repulsive force between them. It may be possible, then, if little kinetic energy is imparted to the CO on photolysis, that the rigid architecture of the pocket and lack of thermal energy of CO at 4 K could balance the repulsive van der Waals forces, leaving the CO close but not bound to the iron.

difference in ligand position may be responsible for the differences in recombination rate constants.

This paper reports the isolation of stable intermediates of MbCO recombination by optical pumping and their characterization with complementary techniques. The results expose novel properties of the myoglobin reaction and delineate a possible trajectory of the ligand and its rebinding to the heme.

Experimental Procedures

Purification of Proteins. (*A*) *Myoblobin* (*Mb*). Myoglobin from sperm whale (type II from Sigma) contains impurities as well as isoenzymes, and purification is employed. Low-salt preparations are needed to avoid artifacts due to the formation of eutectics that scatter X-rays and compromise the low-temperature EXAFS data. First, a desired amount of the protein is dissolved in 0.1 M phosphate buffer, pH 7.0, and dialyzed against the same buffer for 16 h with two to three changes in the cold room (4 °C). Then it is centrifuged in a refrigerated centrifuge at 10000 rpm for 30 min, and the precipitate is discarded. The supernatant, which contains Mb, is further purified essentially according to the method of Rothgeb and Gurd (1978). The pH of the Mb solution is decreased to pH 6.4, and the solution is passed through an ion-exchange column (Whatman CM-52) equilibrated with 0.1 M phosphate buffer, pH 6.5. The major fraction is collected and concentrated in an Amicon Diaflow apparatus to a concentration of 1–5 mM.

(*B*) *Effect of Solvents.* Often, cryoprotectants are added to the samples in order to obtain glasses at low temperature (Chance et al., 1983; Chance et al., 1984) or, in this case, to inhibit eutectic formation on freezing. By using highly purified and salt-free preparations, we are able to obtain acceptable EXAFS data without the use of any cryoprotectant [30% ethylene glycol or 50% glycerol (Chance et al., 1979)]. No differences were observed, however, between samples with and without 30% ethylene glycol in these studies. Fiamingo and Alben (1985) have reported incomplete photolysis with samples containing glycerol glasses even when illuminated for 11 h with a 500-W projection lamp. These samples showed less and less photolysis on recycling.

(*C*) *Effect of pH.* The effects of pH upon the p*K* of buffer systems are largely avoided by the 1–5 mM protein concentration, which is an effective buffer and results in a relatively small pH shift with temperature (Bray, 1964; Chance et al., 1975).

(*D*) *Sample Preparation.* All samples used for low-temperature studies are prepared in the following way: an Mb solution of desired concentration is loaded into the reaction vessel which is kept on ice to eliminate possible protein denaturation during sample preparation. The vessel has four stainless steel tubes connected to it: (i) an inlet tube for Argon (Ar); (ii) an inlet tube for carbon monoxide (CO); (iii) a gas outlet tube; and (iv) a transfer tube with valve.

Initially, Ar is passed over the protein solution with gentle stirring for about an hour. Then a slight excess of a concentrated solution of sodium dithionite is added through the side with a syringe. CO is then passed over the protein solution for at least 30 min. The sample is finally loaded into the sample holder via the following steps. (1) The valve of the transfer tube is opened with sample holder on it, and the gas outlet tube is closed so that the sample holder is flushed with CO. The bottom of the transfer tube is above the meniscus at this time. (2) The transfer tube is plunged into the protein solution with the gas outlet tube still closed. The pressure of the CO gas pushes the protein solution into the sample holder, and as soon as the sample holder is filled with the protein solution, the transfer tube valve is closed. The sample holder is then removed and frozen over a liquid nitrogen bath.

Physical Apparatus. Our studies have employed an Air Products helium cryostat. The sample and reference (buffer) are placed on the Cu cold finger [see Figure 1 of Chance et al. (1983)] inside the chamber. By use of the liquid-transfer helitran system and the temperature controller, any specific temperature in the range from 4 to 300 K can be obtained and held constant (±1 K) by regulation of the heater element as calibrated by a thermocouple implanted in the sample. Our 0.1-mL sample and small Cu holder are found to give a very small gradient (<2 K) between thermal element and sample when the radiation shield is employed. The sample chamber is under vacuum (10^{-4} mmHg) and has mylar windows in each side to allow X-rays to pass. The outside surface of these windows are defogged with N_2 gas. The measuring light comes from a monochromator (600–800 nm) through a 30-Hz oscillating mirror which illuminates sample and reference alternatively and is synchronized with the split-beam detector. The split-beam detector takes the signal from the photomultiplier tube as input, stabilized due to dynode voltage feedback, and gives the ratio of absorption of the sample and reference as output. The continuous light (tungsten lamp) or flash light (xenon flash lamp, 0.2 Hz) can illuminate the sample through the side windows when EXAFS data are not required; the rise in sample temperature is <1 deg. A No. 88A Kodak Wratten gelatin filter allows the photomultiplier tube to record the near-IR absorbance changes, and a No. 4010 Corning Glass filter ensures that minimal sample heating occurs during optical pumping. The absorption spectra can be recorded by scanning transmission spectroscopy (700–800 nm) during continuous illumination [see Figure 1 of Chance et al. (1983)]. The tungsten lamps are water cooled, and the intensity can be continuously adjusted up to 6.8 A (45 W), appropriate for pumping at 40 K. This apparatus was employed for both the kinetic and X-ray absorption and some of the resonance Raman studies.

Combined X-ray, optical pumping, and near-IR absorption spectrophotometry requires sharing of optical pumping and IR monitoring at present. IR monitoring and EXAFS are readily combined via a film of aluminized mylar as shown in Figure 1. Since both side windows of the cryostat are occupied by X-ray detectors in this configuration, optical pumping is alternated with sample monitoring 5 min every 15 min or every 1 h. Optical pumping lamps then occupy the back window, and the X-ray detector positions are as shown in Figure 1 (detailed protocol appears in Figure 4). In order to ensure that the composition of the sample states obtained by optical pumping is maintained during optical monitoring, the sample temperature is abruptly dropped to 4 K as pumping is terminated and the optical spectroscopic measurements take place. After completion of the spectrum (5 min), the pump lamps are replaced, the temperature is ramped to 40 K, and illumination is restored. The region of 7150 eV is examined before and after this "temperature jump" to ensure that the average state of the sample is unaltered (Chance et al., 1983, 1984). This cumbersome procedure is feasible as shown below, providing special attention is paid to rapid temperature jumps. Sacrifices of the X-ray count rate are observed if the MnO_2 filter is moved away from the mylar window of the He cryostat to accommodate the aluminized mylar optical deflector.

Extent of Photolysis. Two criteria for quantifying the extent of photolysis have been employed: optical and X-ray absorption spectroscopies. An optical absorption procedure is to measure a sample of 1.2 mM MbCO, to photolyze it completely at 4 K with multiple flashes from the xenon lamp

with optical and X-ray observation as described above (Chance et al., 1983), and to calculate the extinction coefficient with respect to the MbCO base line or with respect to 740 and 790 nm. Under these conditions, the extinction coefficient of Mb*CO at 4 K is equal to that for the chemically prepared deoxy species (0.9 ± 0.01 cm^{-1} mM^{-1} at 4 K). This value is ~2 times the value given by Fiamingo and Alben (1984).

A second procedure involves continuous illumination on both sides of the sample plus transmission measurements through the sample to ensure quantitative measurement of the sample properties. The absorption of a 1 mm thick 5 mM sample is 1.0 (10% transmission). This assay method, together with white light photolysis, either continuous or flash, which can be operative upon charge-transfer bands beyond 600 nm (Chance et al., 1983), ensures that the sample is uniformly photolyzed and that the degree of photolysis can be accurately determined.

Typical kinetics of an optically pumped sample are shown in Figure 2, where a steady state of photolysis is established by optical pumping at 40 K. The kinetic properties of the population are assayed by turning the pump light off (Figure 2), the measuring light being too dim and at a wavelength of too small an extinction coefficient to cause any significant photolysis. In addition, X-ray monitoring of the sample state at 7150 eV is employed to ensure that X-ray and optical data are congruent.

In our previous work, transmission spectroscopy in the 765-nm region and X-ray fluorescence in the 7160-eV region show good agreement and indicate 90% photolysis with repeated flashes of white light (Chance et al., 1983; Powers et al., 1984). Both the X-ray and optical beams penetrated the entire sample and thus afforded a paragon for measurement of photolysis through the sample [note the correspondence of the X-ray and optical data; see Figure 12 of Chance et al. (1983)]. Fiamingo and Alben (1984, 1985) report that their calculations of amount of photolysis (31–77%) differ from our experimental results (>90%), but they failed to repeat our X-ray or our optical experiments. Their suggestion that IR spectroscopy at 1945 cm^{-1} could be used for sample monitoring under conditions of X-ray observation requires documentation. Our previous and current use of X-ray fluorescence detection and near-IR absorption spectroscopy in transmission for 1–5 mM samples in aqueous solution is adequate to quantify the extent of photolysis within ±5%.

Sample Integrity and Monitoring. Optical monitoring of the states trapped at 4 K is required to ensure sample integrity (Chance et al., 1982, 1983) and a lack of conversion to met-Mb (Fiamingo & Alben, 1985), an accurately measurable concentration of photoproduct needed for X-ray absorption data analysis, and the capability for completion of photolysis at 4 K [repetitive xenon flashing (Chance et al., 1983)] or recombination at >100 K. Optical monitoring of the continuously illuminated sample requires crossed filters (described below) to avoid interference of the excitation and measuring light beams. This is possible with optical monitoring at 765 nm and optical pumping at 500–700 nm. An alternative method of optical assay of the composition (especially at 40 K) is to discontinue illumination, freeze trap the sample state at 4 K, and record without crossed filters. Both methods yield the same result within our error. The latter method avoids any effect of temperature upon the absorption peak.

X-ray Absorption Methods. The X-ray absorption data were collected at the Stanford Synchrotron Radiation Laboratory during dedicated operation of the SPEAR storage ring on beamline II-2. The V-slits were adjusted to provide 2–3-eV resolution with Si111 monochromater crystals at 7–8 KeV. These data were analyzed in the same manner as those described in Chance et al. (1983, 1984), including the model compounds and the constrained amplitude ratio two atom type fitting procedure. A detailed description is also given in Powers et al. (1984).

Resonance Raman Methods. Unlike the optical and X-ray absorption studies, where the amount of photolyzed sample was ~50%, it is observed that, for <40 K, the laser probe provided a nearly completely photolyzed sample. Duplication of the illumination intensity and data collection time used for the optical and EXAFS studies did not produce adequate signal to noise resonance Raman data. However, these conditions were approached so that 8% of MbCO was present at 40 K and 20% was present at 60 K. Since these variations in the amount of photoproduct did not alter the data of the photoproduct, and the degree of photolysis overlaps with that of the optical pumping protocol at higher temperatures, it is very likely that the photoproducts probed in the resonance Raman studies are the same as those of the optical and X-ray absorption studies.

Raman studies were carried out under two conditions both of which yielded the same results: (1) employment of the same cryostat with a continuously variable temperature controller and steady-state illumination optics as were used in optical and X-ray absorption studies, and (2) employment of a Janis liquid helium immersion cryostat from which Raman spectra were obtained at temperatures from 2 to 220 K.

To minimize scattering, optical-quality quartz windows replaced the mylar windows and excitation was obtained with a continuous wave (CW) helium/cadmium laser (4–40 mW, 441.6 nm) focused on the sample to a spot 1 × 2 mm. Using a 90° collection geometry, light scattered from the surface of the sample was collected and focused into a 0.64-m (Instruments SA, Model 640) spectrograph containing a single 2400 groove/mm holographic grating. The output was focused onto an image intensified Reticon (Princeton Instruments) interfaced with an AT&T PC. The frequency was approximately 350 cm^{-1}, and the entrance slit width of 75 μm ensured a resolution of 2–3 cm^{-1}. Stray light interference was minimized by transmission notched filters covering the regions of interest (Barr Associates) at the spectrograph entrance slit. Despite the notch filter, scattered light contributions are occasionally observed in the low-frequency region. Scattering contributions from ice on the sample surface were minimized by multiple temperature cycling (up to 180°), by the use of concentrated samples, and by covering the sample with a 1 mm thick sapphire window while those from the sample itself were eliminated by the addition of ~30% ethylene glycol.

The heating of the sample by the laser beam was determined to cause a 3 K rise in sample temperature at temperatures between 4 and 80 K in the helitran by a thermocouple embedded in the laser-illuminated sample spot. This temperature rise occurred within 5 s of laser illumination and remained constant for the duration of the data collection interval.

RESULTS

Optical Absorption Studies. The λ_{max} is 765 ± 0.2 nm at 40 K, and no shift of the peak is observed on recombination (200-nm focus replica grating monochromator, Bausch & Lomb). Figure 2 gives the apparent ϵ_{765} = 0.62 cm^{-1} mM^{-1} at 40 K and ϵ_{765} = 0.92 cm^{-1} mM^{-1} at 4 K while the chemically prepared deoxy compound gives ϵ_{758} = 0.80 cm^{-1} mM^{-1} at 4 and 40 K (the ϵ values are referenced to 740 and 780 nm).

The analysis of the kinetics at 765 nm of the optically pumped samples follows. In order that a more homogeneous

Table I: Effect of Illumination Time on Kinetics of Recombination[a]

illumination time (min)	extent of photolysis (%)[b]	extent of recombination (%)[c]	k_{slow} (s^{-1})	A_{slow}	k_{fast} (s^{-1})	A_{fast}	mean deviation
20	39	30	2.55×10^{-5}	0.835	1.22×10^{-3}	0.125	1.30×10^{-2}
40	37	25	1.83×10^{-5}	0.855	1.17×10^{-3}	0.125	7.39×10^{-3}
73	45	24	1.32×10^{-5}	0.836	1.12×10^{-3}	0.148	6.80×10^{-3}
112	43	20	1.11×10^{-5}	0.861	1.52×10^{-3}	0.115	9.20×10^{-3}

[a] Temperature was 40 K; data measured over a 2-h interval. [b] Based on the total sample. [c] Based on the extent of photolysis.

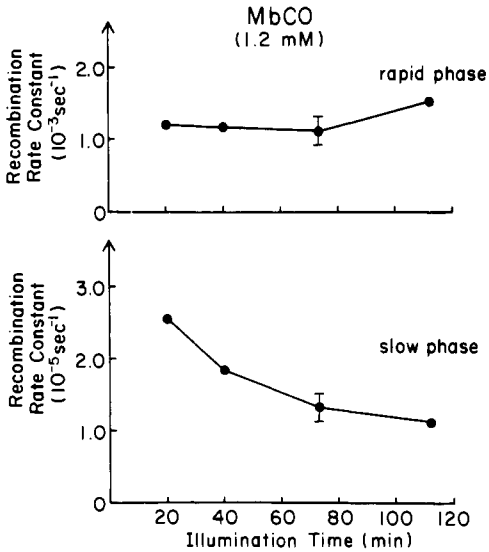

FIGURE 3: Effect of illumination time upon the optical pumping of MbCO (1.2 mM) (see Figure 4 protocol). The occupancy of the sample by the slow phase under these conditions is indicated by Table I, as is the validity of the fit to the two-component model.

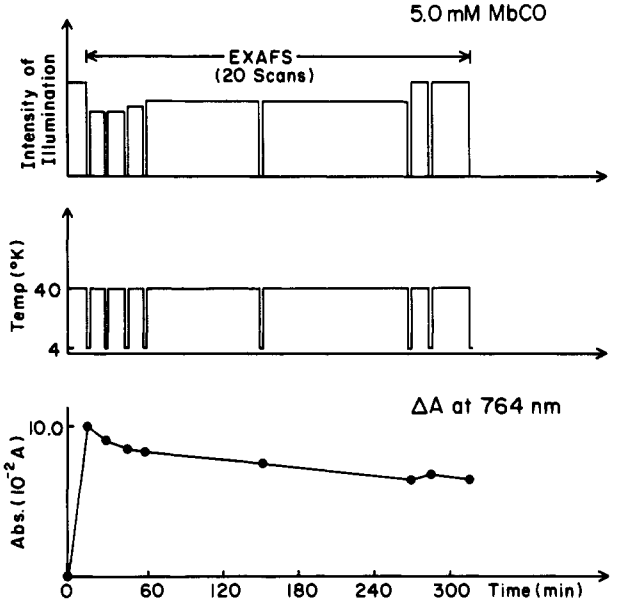

FIGURE 4: Protocol for optical pumping of MbCO (5 mM) with time sharing of optical monitoring and X-ray absorption spectroscopy.

population be studied, we adjust the optical pumping rate to give ~50% of the sample recombined as MbCO, which represents a portion of the preparation that recombines rapidly. The more slowly recombining portion is the object of our study, and the extent of reaction given below refers to the ~50% photolyzed portion. The kinetics of recombination of the 765-nm band of this ~50% photolyzed portion is followed for several hours so between 20% and 75% recombination has occurred in this time. Over this four decades of time, it is difficult to distinguish power law kinetics and a sum of two exponentials since mathematically a power law is generated by integration or summing exponentials (Austin et al., 1975). The differences are smaller than the error in the data. The kinetics data are fitted within the error by two phase kinetics that differ by about 100-fold in rate. This representation is chosen for two reasons: it distinguishes the kinetic differences in the main populations isolated by optical pumping, and although the data can be described by a power law, it requires a different activation enthalpy distribution than that reported for the single flash recombination data for 10^{-5}–1 s (Frauenfelder, 1985).

Our data were fit as the sum of exponentials:

$$A = A_{slow}e^{-k_{slow}t} + A_{fast}e^{-k_{fast}t} \quad (1)$$

where slow denotes Mb* at $t = 0$. The value A_{slow} for the slow phase is given in fractional terms (A_{fast} being $1 - A_{slow}$) together with the mean deviation (<1%) for four illumination times in Table I (Figure 3). The data are fit within the signal to noise with two components, indicating that the two photoproduct populations were trapped by optical pumping in concentrations >5% of the sample. Similar results were obtained when the sample concentration was lowered to 25 μM (Chance et al., 1987). The slow phase has an amplitude A_{slow} that is 86% (of 49%) "slow" as obtained by optical pumping at 40 K. The decrease of k_{slow} with time shown in Table I (Figure 3) identifies the formation, by prolonged illumination of Mb*, of a more slowly recombining form which we term Mb**.

In summary, at 40 K the optical pump rate allows the faster phase(s) to recombine (51% of the sample). The remainder consists of a slow phase (Mb*) which is converted into an even more slowly recombining form (Mb**) that accounts for 43% of the sample, and 6% recombines at an intermediate rate.

Optically Pumped Steady States. In our spectroscopic study, we employ MbCO and ~50% photoproducts. For simplicity, we do not distinguish MbCO from the 4 K intermediate Mb*CO, and thus we identify the $k = 10^{-5}$ s^{-1} with a population that is maintained nearly completely photolyzed by dual tungsten lamps illuminating each side of the sample. The actual intensity is much greater than that corresponding to 10^{-5} s^{-1} but less than that corresponding to 10^{-3} s^{-1}. Thus the system is turning over with optical pumping more slowly than 10^{-3} s^{-1} and faster than 10^{-5} s^{-1}. These values of kinetic constants justify that 1-min freeze trapping time is adequate for the 40 K optically pumped state (Mb**).

X-ray Absorption Studies. (A) Optical Controls. Figure 4 illustrates the time sequence of events of the X-ray absorption spectroscopic protocol that is based upon the preceding discussion. This protocol allows acquisition of the X-ray absorption data on Mb** employing manually regulated optical pumping in response to optical measurements of the 765-nm band. The events during the protocol are indicated by the three scales indicating intensity of illumination, temperature of the sample, and optical signals.

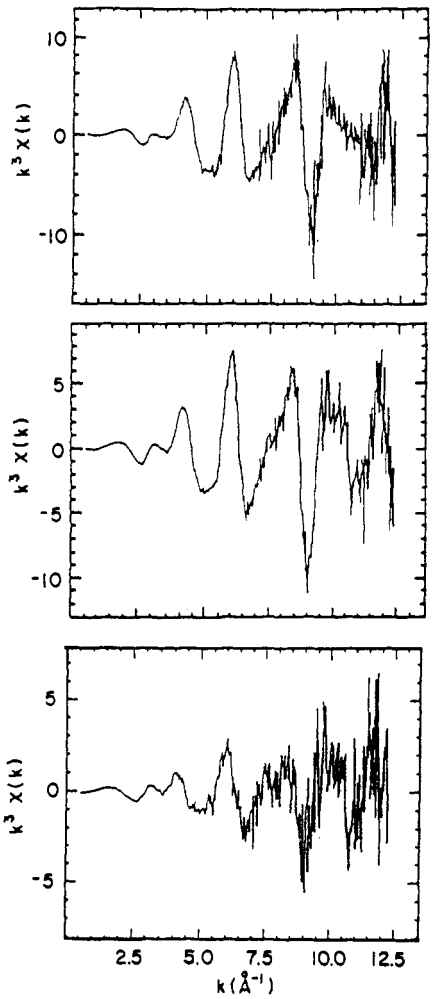

FIGURE 5: (Top) Background-subtracted, k^3-multiplied data at 40 K of MbCO normalized to one Fe atom, (middle) optically pumped sample containing 40% photolyzed component (Mb**) normalized to one Fe atom, and (bottom) Mb** normalized to 0.4 Fe atom (difference between middle and top data).

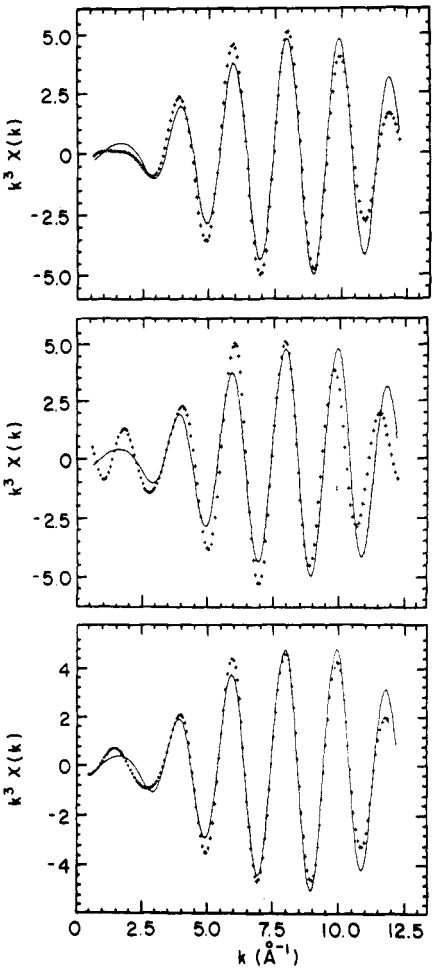

FIGURE 6: First shell filtered data for the slowly recombining state Mb** at 40 K (—) normalized to one Fe atom compared to that of (top) MbCO (+++), (middle) deoxy-Mb (+++) and (bottom) Mb*CO (+++).

The experiment indicates initial high-intensity illumination, causing photolysis of MbCO to the Mb* state with an absorbance change measured with respect to MbCO of 0.10, corresponding to 50% photolysis. Optical monitoring is accomplished by freeze trapping of the sample at 4 K every 15 min during the first 1 h (some decrease of the photoproducts, 10% for the 15- and 30-min points, was found, so the intensity of illumination was increased). Since the subsequent two points (45 and 60 min) showed little change, the illumination at a slightly higher level was continued for an interval of $1^1/_2$ h, during which time X-ray data were accumulated. Since the sample has already been illuminated for 60 min, the bulk of the change from Mb* to Mb** indicated in Figure 3 had occurred, and thus X-ray absorption spectroscopy in the subsequent $1^1/_2$-h interval of optical pumping corresponded to a nearly homogeneous population of Mb** together with MbCO. At the end of a second interval of data accumulation of 2 h, a further decline of 15% of the Mb** form had occurred. At this point, increasing the pump light restored the population to a constant population of photoproduct, as monitored by optical absorption.

(*B*) *Data Analysis Procedures.* X-ray absorption data were collected at 40 K on MbCO and deoxy-Mb, as well as optically pumped samples (containing Mb** and MbCO). In the latter, the amount of Mb** was determined by optical absorption spectroscopy as described above, and the appropriate amount of MbCO was subtracted from the X-ray data in two ways, both of which yielded the same results. First, the background-subtracted, k^3-multiplied data of MbCO were subtracted in the appropriate quantity from that of the optically pumped sample data as shown in Figure 5. The result was then Fourier transformed, the first shell filtered, and back transformed. In an alternate procedure, the appropriate MbCO contribution was subtracted from the first shell filtered data of the optically pumped samples as shown in Figure 6. Both subtraction methods gave identical first shell filtered data for Mb** within the error. The first shell filtered data was fit by using the two atom type procedure with fixed amplitude ratios, and then the amplitudes were allowed to vary. The goodness of fit was judged by the sum of residuals squared ($\sum R^2$). The fitting error was determined by changing each parameter with the others held fixed until the sum of residuals squared doubled in value on each side of the minimum. The error of ±5% in the optical absorption data which determined the amount of Mb** in the sample was taken into account in the subtraction procedures by adding (and subtracting) 5% to (and from) the MbCO contribution. The result for both extremes was then fit as described above and the fitting error determined. The difference between the parameter values for the extremes was then appropriately combined with the fitting error to determine the total error. Four such data sets using four different samples having photolyzed components ranging from 55% to 20% were collected and analyzed individually. All gave the same parameter values for Mb** in the two atom fitting procedure within the error. These Mb** data were then

Table II: Results of Fitting Parameters for Photoproducts

parameters	Mb*CO (4 K)[a]			Mb** (40 K)		
	r (Å)	N	$\Delta r^2 \times 10^3$ (Å^{-2})	r (Å)	N	$\Delta r^2 \times 10^3$ (Å^{-2})
Fe–N_p	2.03 ± 0.01	4	5.0 ± 1	2.04 ± 0.007	4	5.3 ± 1.5
Fe–N_e	2.22 ± 0.02	1	4.3 ± 1	2.20 ± 0.01	1	6.6 ± 2.0
Fe–C	1.97 ± 0.02	1	3.0 ± 2			

[a] Taken from Chance et al. (1983) and Powers et al. (1984).

averaged and fit with the two atom type procedure, and the total error was determined.

*Structure of the Mb** Geminate State.* First, comparison of the control samples, MbCO and deoxy-Mb at 40 and 4 K, is necessary in order to compare photoproducts accumulated at these temperatures. The first shell filtered data for MbCO at 40 and 4 K as well as that for deoxy-Mb are identical within the error at the two temperatures: $\Delta r = 0.002 \pm 0.01$ Å, $\Delta N = 0.13 \pm 0.15$, and $\Delta\sigma^2 = -0.001 \pm 0.0008$ Å^{-2}.

The data collected by this protocol yielded excellent signal to noise data for the optically pumped samples and are shown in Figure 5. The first shell filtered data of Mb** after normalization to one absorbing atom is shown in Figure 6 and compared to MbCO and deoxy-Mb at 40 K as well as the photoproduct as 4 K, Mb*CO, reported previously (Chance et al., 1983). It is clear that the structure of the first coordination shell of this slow phase is different from any of these. The structure is, however, more like Mb*CO, especially in phase; the differences are largely in amplitude.

The results of the two atom type fitting procedure on the Mb** component are shown in Table II, where they are compared to those for Mb*CO (Chance et al., 1983; Powers et al., 1984). Only one solution having physically reasonable parameters (Powers et al., 1984) was found, and this solution produced a sharp well-defined minimum. Within the error, the iron to pyrrole nitrogen distance (Fe–N_p) of Mb** is identical with that of Mb*CO as is the iron to proximal histidine distance (Fe–N_e). However, no contribution of a sixth ligand (CO) was found in the first coordination shell of Mb**. In fact, the addition of any sixth ligand to the fitting procedure (Powers et al., 1984) causes the $\sum R^2$ to increase by a factor of 15. When the number of the sixth ligand, which was initially set at 1, was allowed to vary, this parameter was reduced to 0.05 and the $\sum R^2$ decreased. The value of the change in Debye–Waller factors $\Delta\sigma^2$ ($=\sigma^2_{\text{model}} - \sigma^2_{\text{protein}}$) for Mb** is not significantly different from those found for Mb*CO. In fact, subtraction of the first shell filtered data of Mb** from that of Mb*CO (Chance et al., 1983) gave a single low-Z (carbon) contribution (within the signal to noise) at 1.97 ± 0.04 Å from the iron. The fact that this difference produces the same contribution, as was found by fitting models to the Mb*CO data, argues that the differences between Fe–N_p and Fe–N_e of the two photoproducts is small and probably not larger than the respective errors (Table II). Thus, we conclude that the only significant difference in the first coordination shell between the photoproduct at 4 K (Mb*CO) and the Mb** at 40 K is the absence of the C of the CO ligand in the first coordination shell of the latter. In addition, this five-coordinate structure of the slow phase at 40 K (Mb**) is very unlike deoxy-Mb (Powers et al., 1984), having a 0.10 ± 0.03 Å difference in the Fe–N_e distance, even though the average Fe–N_p distances are within the error.

The question of whether the photolyzed CO ligand is observed in the higher coordination shells of Mb** is difficult to determine uniquely. In the higher shells of MbCO and Mb*CO, a well-defined low-Z (atomic number; e.g., C, O, or N) contribution is found at 2.78 ± 0.2 and 2.62 ± 0.02 Å, respectively, together with the partially resolved heme and proximal histidine contributions (Powers et al., 1984). Since the first-shell contributions of the heme and proximal histidine are the same within the error for Mb*CO and Mb**, and these are rigid ring structures, the same partially resolved heme and proximal histidine contributions that were found for Mb*CO (Powers et al., 1984) can be used to represent those of Mb**. When these higher shell contributions were subtracted from the Mb** data, two well-defined low-Z (C, O, N) contributions were found at 2.58 ± 0.04 and 3.42 ± 0.06 Å. It is surprising that these contributions are so well-defined, especially at such long (nonbonding) distances from the iron. It is, however, difficult to interpret these as heme or proximal histidine contributions since the latter occur at 3.0 and 4.13 Å in all heme proteins studied (Powers et al., 1984). Examination of the crystallography data of myoglobin indicates there is no contribution from other residues at these distances. Thus, we are left with attributing these two contributions to the CO molecule. If these are the distances of the C and O of the CO molecule, then the Fe···CO angle is 135–145° [taking the C–O distance as 1.05 Å (Powers et al., 1984)], and the ligand position is rigid with respect to the iron although it has moved ~0.7 Å away from its bound position in MbCO.

Resonance Raman Studies. At all experimental temperatures between 1.2 and ~200 K, the Raman spectrum of the photoproduct indicates a five-coordinate high-spin Fe^{2+}. Between 1.6 and ~160 K, the frequency of the porphyrin π-electron sensitive mode ν_4 for the photoproduct is ~1 cm^{-1} lower in frequency than for equilibrium deoxy Mb (~1355 cm^{-1}) at the same temperature The line shapes are, however, identical with the experimental error. At the higher temperatures studied, evidence for an increased rate of ligand recombination becomes apparent in that ν_4 for MbCO (~1375 cm^{-1}) grows into the spectrum at the expense of the 1355-cm^{-1} peak. In time-sequence studies of continuously illuminated MbCO at higher temperatures (80–160 K), several minutes are required before a steady-state mixture of five- and six-coordinate species is reached on the basis of the evolving 1375/1355 cm^{-1} ratio for ν_4. At the lower temperatures ν_2, the core marker, is asymmetrically broadened and skewed toward lower frequency, relative to deoxy-Mb (Figure 7), as previously reported (Rousseau & Argade, 1986). ν_2 exhibits little change with temperature between 2 and ~100 K, but the difference between the photoproduct and deoxy-Mb decreases appreciably at temperatures above 100 K similar to the behavior of ν_{vinyl} (Figure 7). The frequency of $\nu_{\text{Fe-His}}$ in the photoproduct is shifted by 5 cm^{-1} to higher frequency compared to deoxy-Mb at temperatures between 2 and 100 K (see Figure 8). Above 100 K, this difference decreases progressively with increasing temperature, and by 220 K no difference is observed within our error. Below 100 K, $\nu_{\text{Fe-His}}$ for deoxy-Mb is shifted to higher frequencies than the 300 K spectrum and is temperature invariant in this region. Above 100 K, however, it begins to shift toward the 300 K value. Although $\nu_{\text{Fe-His}}$ for both the photoproduct and deoxy-Mb does not exhibit any shift in frequency with temperatures below 100 K, the intensity for the photoproduct exhibits a systematic enhancement with temperature between 2 and 100 K. Two kinds of intensity changes of $\nu_{\text{Fe-His}}$ are observed in the photoproduct. The first, which was previously reported by Sassaroli et al. (1986), is an irreversible increase occurring at the lowest temperature (2–20 K). If MbCO is illuminated and heated with a 20-mW excitation (441.6 nm) at 2 K, a sequence of 1-min spectra shows a progressive increase in the intensity

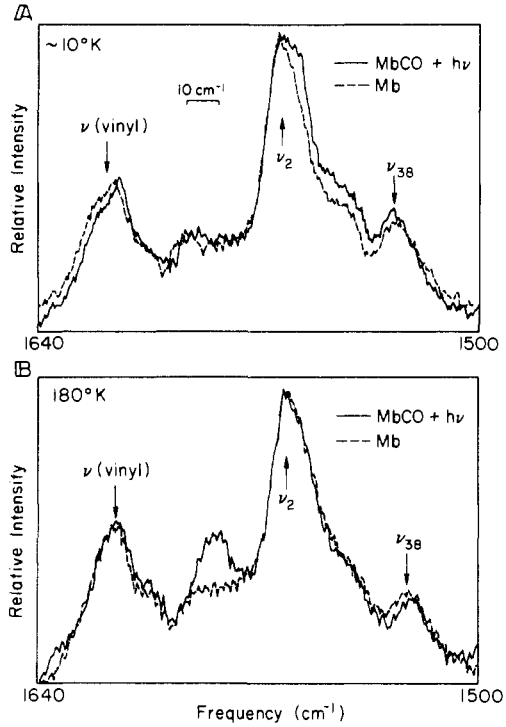

FIGURE 7: High-resolution comparison between chemical deoxy-Mb (---) and the photoproduct of MbCO (—) in the region of ν_2 and ν_{vinyl}. The line shape differences between deoxy-Mb and photoproduct for ν_2 and ν_{vinyl} seen at 10 K persist until ~100 K. It can be seen that at 180 K there are minimal differences between the photoproduct and deoxy-Mb. The peak seen at ~1590 cm^{-1} for the photoproduct at 180 K is due to MbCO. This peak starts to become prominant at 60 K, presumably reflecting an increase in the rebinding rate relative to the photodissociation rate.

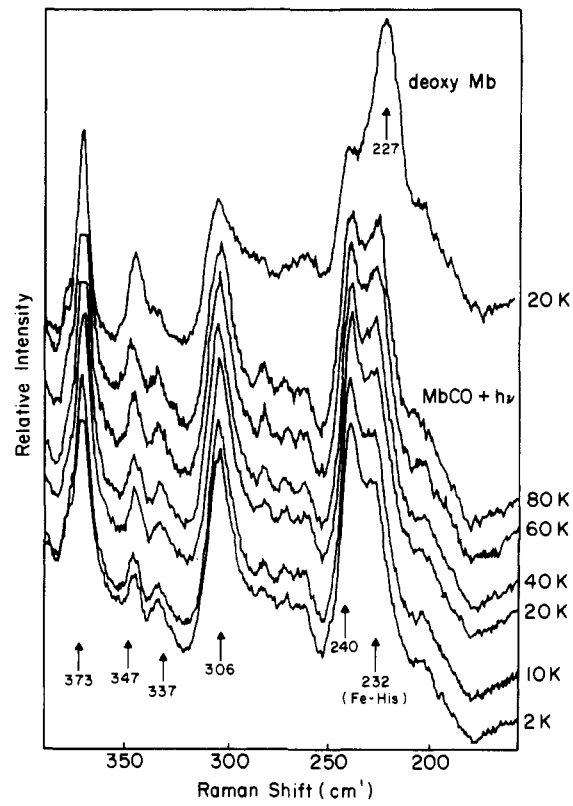

FIGURE 8: Effect of temperature upon the low-frequency region of the Raman spectrum of the MbCO photoproduct. Each spectrum is the result of a 5–10-min average using a 1 × 1 mm laser probe (4417 Å, 20 mW). Also shown (top) is the corresponding spectrum of deoxy-Mb. The spectrum of deoxy-Mb does not show appreciable temperature effect below 100 K. Both samples were dissolved in a 30% ethylene glycol–water mixture.

of ν_{Fe-His}. The first spectra in the sequence resemble the low-power (2-mW) spectrum reported by Sassaroli et al. (1986). The intensity change is not reversible, and a decrease in laser intensity or sample temperature does not restore the original spectrum unless the sample is first annealed at greater than 120 K. In addition, there is a reversible intensity change with temperature (2–100 K), which is shown in Figure 8. In this case, dropping the temperature from 100 to 20 K, for example, results in the reappearance of the initial 20 K spectrum. In the temperature range 2–100 K, other differences between the photoproduct and deoxy-Mb do not change appreciably. As with the frequency differences in ν_{Fe-His} and ν_2, other differences, such as the doublet at 338–345 cm^{-1} (Figure 8), do not begin to change until >100 K.

In summary, the frequencies in the Raman spectrum of the MbCO photoproducts do not change between 2 and 40 K. The only effect of temperature is the progressive change of the ν_{Fe-His} intensity. The spectrum of the photoproduct is, however, different from that of deoxy-Mb, as summarized in Table III. These differences are maintained up to 100 K, at which point further increase in temperature results in frequency changes in both deoxy-Mb and the photoproduct.

Table III: Comparison of Resonance Raman Data of the MbCO Photoproduct and Deoxy-Mb

	photoproduct		
marker	1.2–10 K (Mb*CO − Mb) (cm^{-1})	10–100 K (Mb** − Mb) (cm^{-1})	>100 K
ν_2 (core size)	line shape difference	line shape difference	approaches 0
ν_{Fe-His} (proximal histidine)	irreversible intensity change, +~5	reversible intensity change, +~5	approaches 0
ν_{vinyl} (vinyl)	line shape difference	line shape difference	approaches 0
ν_{38}	+~2	+~2	approaches 0
ν_4 (π-electron density)	−1	−1	approaches 0

Discussion and Conclusions

Several models for the reaction of Mb with CO have been proposed (Alberding et al., 1976a,b; Marden, 1982), and most have been applied to modeling the data of Frauenfelder and co-workers (Ansari et al., 1985; Austin et al., 1975; Frauenfelder, 1985) in the short time regions. We have focused on the isolation of intermediates, whose structural differences may be indicative of the different barriers for recombination. These intermediates are maintained in a steady-state concentration by continuous illumination (optical pumping), and in this respect, the spectroscopic studies reported here differ from those of transient states reported previously (Ansari et al., 1985; Austin et al., 1975; Frauenfelder, 1985). Thus, we report three distinct geminate states observed under conditions of optical pumping.

The Geminate States. At ~4 K, a geminate state, Mb*CO, is accumulated by optical pumping, and previous X-ray absorption measurements show that while the nitrogen of the proximal histidine distance is unchanged from that of MbCO, the CO is in close proximity to the iron of the heme but is not bound (Chance et al., 1983; Powers et al., 1984). The Fe···C distance is changed by ~0.05 Å, and the Fe···CO angle is decreased by ~10–15°, reducing the overlap of the σ orbital of CO with the $3d_{z^2}$ orbital of the iron heme. The iron has moved 0.35 ± 0.07 Å out of the heme plane, ~0.1 Å less than

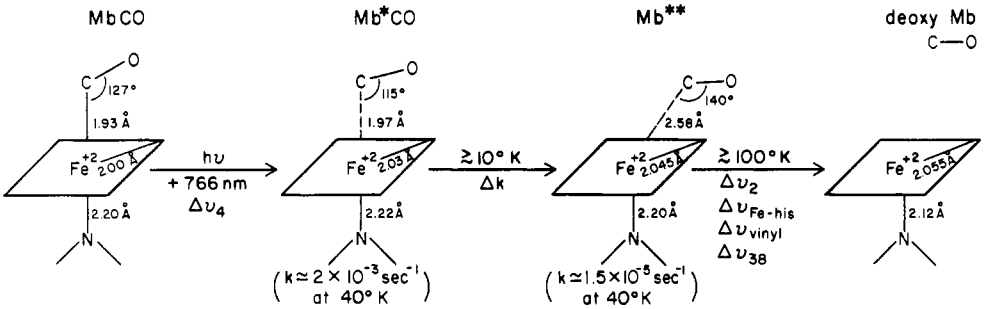

FIGURE 9: Summary of the structures and properties of the geminate states in the photolysis of CO-bound myoglobin at low temperature. Each state was optically pumped in the temperature range indicated and investigated by optical absorption (766-nm band), X-ray absorption, and resonance Raman spectroscopies. Bond distance and angle errors are given in Table II. The changes in physical parameters that denote the states are listed below the arrow: (+) denotes appearance and (Δ) indicates a change. ν's refer to the resonance Raman markers. See text for complete discussion.

deoxy-Mb (Chance, B., et al., 1983, 1984, 1986; Chance, M., et al., 1986).[3] This localized configuration might be the most rapidly recombining geminate state observed at 40 K, having a rate of $k_1 \sim 2 \times 10^{-3}$ s^{-1}, or may recombine even faster and is not kinetically isolated by the conditions of optical pumping. The average Fe–N_p distance is 2.03 ± 0.01 Å and is distinguishable from those of MbCO at 2.00 ± 0.01 Å and deoxy-Mb at 2.06 ± 0.01 Å. The ν_2 core-size (Ct···N_p) marker and ν_4 are shifted to lower frequency than that of deoxy-Mb by 2–3 and 1 cm^{-1}, respectively. The iron–proximal histidine linkage is clearly different from that in deoxy-Mb. No change is found in the Fe–N_e distance between MbCO and Mb*CO geminate state (2.22 ± 0.02 Å), remaining ~0.10 Å longer than that of deoxy-Mb. Thus, in the localized configuration (Mb*CO), the heme core is perturbed but the proximal histidine is the same distance from the iron as in the ligated state but less strained relative to deoxy-Mb, as reflected in the higher frequency of $\nu_{Fe\text{-}His}$. The out of plane heme distortions may differ from deoxy-Mb, as does the porphyrin vinyl group, but the overall porphyrin π-electron density is similar to that of deoxy-Mb.

At ~40 K, two geminate states, Mb* and Mb**, are accumulated by optical pumping that are more slowly recombining than Mb*CO and differ from each other by ~3 in their temperature-dependent recombination rates ($k_2 \sim 3 \times 10^{-5}$ s^{-1} and $k_3 \sim 1.1 \times 10^{-5}$ s^{-1} at 40 K, respectively). The slowest phase, Mb**, differs from Mb*CO in that the dissociated CO has moved at least 0.7 Å away from its ligated position. Although the average Fe–N_p distance is 2.045 ± 0.007 Å, within the error of that for both Mb*CO (2.03 ± 0.01 Å) and deoxy-Mb (2.055 ± 0.08 Å), the ν_2 core marker is unchanged from that of Mb*CO. The Fe–N_e distance is within the error of that found for Mb*CO (~0.10 Å larger than that for deoxy-Mb), and the $\nu_{Fe\text{-}His}$ frequency is also identical. It is plausible that the irreversible heating induced intensity change in $\nu_{Fe\text{-}His}$ first reported by Sassaroli et al. (1986) is due to the shift in the position of the ligand that is observed in the EXAFS studies which occurs between 4 and 40 K. Support of this interpretation comes from the observation that these intensity changes in $\nu_{Fe\text{-}His}$ do not occur for the photoproduct of *n*-butyl isocyanide and Mb (Campbell & Friedman, 1987). Since *n*-butyl isocyanide differs from CO in that it is considerably less mobile and therefore less likely to shift in position at these cryogenic temperatures, the movement of the iron out of the heme plane is not a likely cause of these intensity changes since neither ν_4 nor the core-sensitive marker ν_2 appears to shift over this temperature region. Thus, in summary, the structure difference between Mb** and Mb*CO is that Mb** has a more distant CO configuration (~0.7 Å away from its close position in Mb*CO and the ligated state). Both, however, are significantly different from deoxy-Mb.

Above ~100 K, substantial changes are observed. The kinetic parameters are too fast to be investigated with the optical and X-ray absorption methods described here. However, in the 100–200 K temperature range, resonance Raman measurements which optically pump the sample because of the high intensities show that all the markers approach the deoxy values for temperatures >~100 K. It appears that deoxy-Mb is not produced by photolysis in an amount that can be measured by our spectroscopic techniques for temperatures <100 K. Figure 9 summarizes the above discussion.

Molecular Mechanism and CO Trajectory. In order to consider the molecular mechanism of geminate-state formation or the trajectory of the dissociated CO, the local structures and properties of the iron heme discussed above must be viewed in the context of other structural aspects of the protein, especially the pocket and the F-helix linkage to the proximal histidine. Kuriyan et al. (1986) have determined a high-resolution (1.5-Å) crystal structure of MbCO at 260 K, and this structure may represent the pocket region of the protein at 40 K from the following considerations.

It is a reasonable assumption that the CO conformations at the temperatures of the X-ray absorption studies (4–40 K) are at least as localized as those at 260 K found by the crystallography study. Even though X-ray absorption spectroscopy cannot determine the orientation of the CO in the pocket or with respect to the heme, the angle it makes with iron determined in our previous studies, 127 ± 4° (Chance et al., 1984), is in excellent agreement with these results as are the Fe–C, Fe–N_e, and average Fe–N_p distances (Table II; Chance et al., 1983; Powers et al., 1984). Crystallography studies of met-Mb at 300 and 80 K (Hartmann et al., 1982) indicate that the overall structure of the protein is very similar at the two temperatures. The unit cell volume decreases by 4.5%, and helices are significantly shorter at 80 K. Even at 300 K, the distal-side residues, especially those forming the pocket as well as the Fe atom and heme group, are quite rigid and have nearly temperature independent atomic mean square displacements. The distal histidine (His-64) which blocks the ligand channel into the pocket is the exception and exhibits significant thermal motion. At both temperatures, the proximal side is less rigid than the distal side with the largest temperature-dependent displacement occurring in the F-helix. In MbCO at 260 K (Kuriyan et al., 1986), both the proximal and distal sides appear quite rigid. Thus computer graphics modeling (Jones, 1982) was used, in collaboration with J. Kuriyan, which employed their atomic coordinates of MbCO at 260 K.

This crystallography study identifies two major conformations of CO, one of which makes an ~141° angle with iron

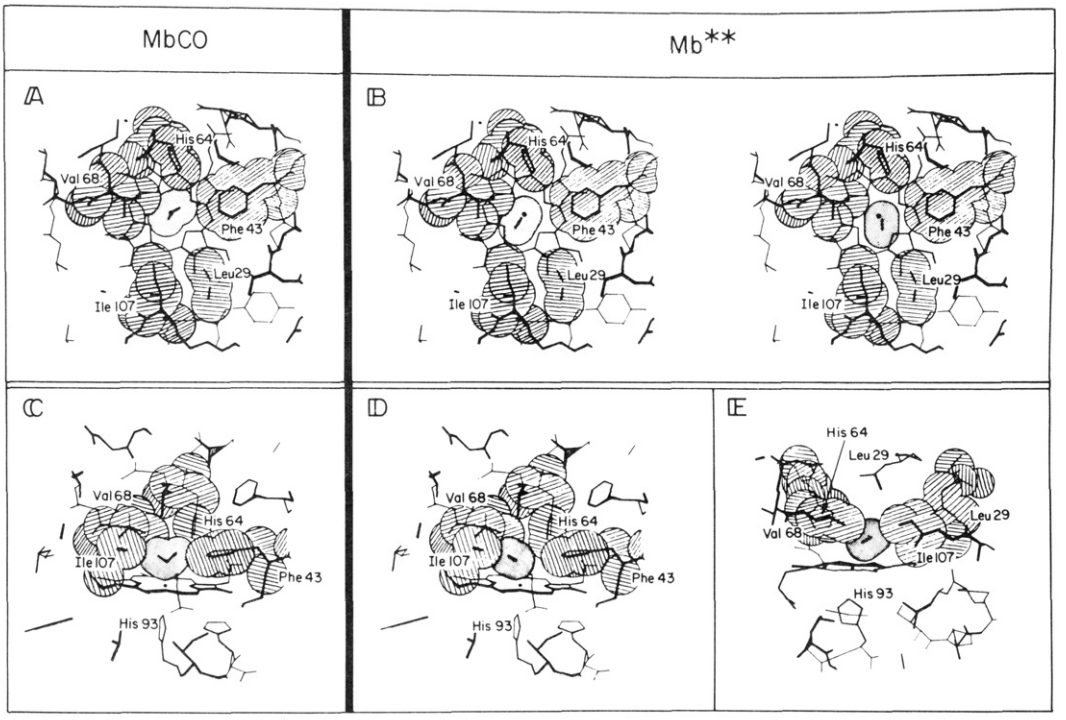

FIGURE 10: Computer graphics simulation of the pocket in myoglobin using the crystallographic coordinates of Kuriyan et al. (1986) and Kuriyan (1986) and the graphics program FRODO (Jones, 1982). The CO molecule is shown gray. Structure of MbCO at 4 (Chance et al., 1983; Powers et al., 1984) and 40 K showing CO positions as found by Kuriyan et al. (1986) and Kuriyan (1986): (A) distal side looking down onto the iron heme and (C) normal to heme plane viewed between Leu-29 and Phe-43. Structure of Mb** with Fe–N_p, Fe–N_e, and Fe···CO reported in this study including CO in crevice formed by Val-68, Ile-107, Leu-29, and Phe-43: (B) distal side looking down onto the extreme positions of CO in the crevice allowed by van der Waals interactions, (D) normal to heme plane viewed between Leu-29 and Phe-43, and (E) normal to heme plane viewed between Val-68 and Ile-107.

and is oriented somewhat toward His-64 (distal histidine) and the ligand channel. This position represents ~75% of the MbCO population. The remaining population is in the second conformation which is rotated ~120° from the first toward the inside of the pocket and Ile-107, making an ~120° angle with iron. These CO conformations are shown in the simulation of Figure 10A,C.

In the higher shells, two well-defined contributions (2.58 ± 0.04 and 3.42 ± 0.06 Å) are found in the X-ray absorption data for Mb** which are likely due to the CO molecule. Thus, the Fe···CO angle is 135–145° [taking the C–O distance as 1.05 Å (Powers et al., 1984)], and in addition, the CO has moved ~0.7 Å away from its bound state position to a position where it is constrained such that large disorder does not exist in the Fe–C and Fe–O distances. Such constraint in the CO position could result from residues defining the pocket. Kuriyan et al. (1986) described a crevice in the pocket that extends into the protein and has sharp potential energy boundaries arising from Val-68, Ile-197, and pyrrole 3 of the porphyrin (Figure 10A,C). By use of the distances found for the higher shell contributions, together with the Fe–N_p from the X-ray absorption studies for Mb**, the computer graphics simulation shows that a CO molecule with these distances can comfortably be placed in this crevice and is constrained to rotate no more than ~20° in any direction (Figure 10B,D,E). The crevice is just large enough for the CO molecule end-on as might be expected if it simply drifted away from the latter (second) of the two bound positions in MbCO.

Since the first orientation which represents ~75% of the MbCO population is ~120° away from the crevice, it is difficult to understand how this population could form Mb** (CO in the crevice) at these low temperatures. Thus, the orientation of the CO may serve as "structural partition"; only the bound CO population having a CO orientation toward the crevice forms Mb** immediately on photolysis. The remainder of the bound CO population may form Mb* having a less constrained CO that finds the crevice only after a period of time. Thus, the kinetic behavior of the CO recombination at low temperature, and hence the observed geminate states on photolysis, may be determined largely by the architecture of the pocket. This is consistent with the fact that there is no observed difference in the optical absorption between Mb* and Mb**: their structures are identical except for the location of the dissociated CO in the pocket, a feature only detectable by X-ray absorption studies.

Protein Coordinate as a Function of Temperature. Below ~100 K, the ν_{Fe-His} and ν_{vinyl} of deoxy-Mb also exhibit a shift to higher frequency compared to the 300 K values. This suggests a temperature-dependent structural rearrangement of the heme and protein. Agmon and Hopfield (1983) have proposed a separate coordinate, in addition to the reaction coordinate, that could describe such rearrangements. Over temperature regions in which no rearrangement occurs Arrhenius kinetics would be observed, but over temperature regions in which there are protein rearrangements simple kinetic theory breaks down.

The results of photodissociation studies at high temperatures (300 K) are also relevant here. Martin et al. (1983) have shown that photodissociation of CO-bound myoglobin occurs within the photolysis pulse duration of 250 fs at 307 nm, and the transient high-spin species produced relaxes with a time constant of 350 fs to deoxy-Mb with optical absorption probes at 422.5 and 438 nm. Findsen et al. (1985) have shown that within 25 ps the ν_{Fe-His} has relaxed to its deoxy-Mb value while Dasgupta et al. (1985) find that at 25 ps the ν_{10}, ν_{19}, and ν_{11} (core markers) are not relaxed to the deoxy-Mb value and remained unrelaxed until ~100 ps. Thus, the picture which emerges is that although photodissociation of the CO ligand and the electronic rearrangement occur within a few picoseconds at 300 K and the proximal histidine has relaxed to

deoxy-Mb by 30 ps, the core (Ct···N) relaxation requires more than 3 times as long. These results are in sharp contrast to those found at low temperatures where neither the proximal histidine nor the core is fully relaxed below ~100 K. The proximal histidine remains unchanged until ~100 K where it begins to relax to deoxy-Mb, just the opposite of the sequence of events at 300 K and short times. Perhaps rearrangement in the protein architecture as a function of temperature plays a role, and kinetic models may need to consider additional degrees of freedom provided by the protein.

Control of Reactivity in Hemoproteins. The unique phenomenon of chemical kinetics in biological systems at helium temperatures has been provided by two different examples: (1) the tunneling of electrons from cytochrome *c* to the photosynthetic reaction center as observed in studies of DeVault and Chance (1966) and (2) the rebinding of CO to the iron atom of Mb as observed initially by Iizuka et al. (1974a) and studied in detail by Frauenfelder and his colleagues (Ansari et al., 1985; Austin et al., 1975; Frauenfelder, 1985). A significant temperature-independent region was observed to 100 K in electron tunneling in photosynthetic bacteria (Devault & Chance, 1966) and to approximately 20 K in nuclear tunneling in MbCO (Alberding et al., 1976a,b, 1978; Marden, 1982). The determination by direct physical methods of the tunneling distance parameters was recently solved by X-ray crystallography in the case of the photosynthetic reaction center where predicted tunneling distances of 28 Å (Alberding et al., 1978) were found actually to be 22 Å by crystallography (Diesenhofer et al., 1985). In the case of myoglobin, the ligand–metal atom distance could have various values depending upon places within the pocket from which the ligand may tunnel to the iron atom. We have found two positions at which the ligand may be retained on its way through the pocket to the iron atom of Mb.

These two positions which are occupied in the reverse of the binding trajectory are quite properly near the heme iron, with the carbon of CO at 1.97 and 2.58 Å away, respectively. There may well be other positions in the heme pocket at which the ligand may be retained in its trajectory to the iron atom. So far, we have considered only one CO molecule within the heme pocket since even one molecule of CO has restricted movement within van der Waals contacts (Kuriyan et al., 1986) of the pocket. The entry of the ligand into the heme pocket may require the help of dynamic protein fluctuations, e.g., breathing, etc., and such motions periodically open structural features to the multitude of colliding CO molecules. In such "breathing" modes, these structural features may provide additional positions that can be occupied by the CO molecule.

Relationship to Enzymology. The important result of this study is the identification of two sites for the CO molecule, one of which is very close to the site occupied by the ligand when bound to the iron (Mb*CO) and the other of which is displaced from it by 0.7 Å and located in a particular crevice of the protein (Mb**). The concept of such sites in enzyme–substrate reactions is a novelty. Ever since the Michaelis and Menten (1913) hypothesis, the substrate binding site has been considered to be the functional site in enzymatic catalysis and ligand binding, even abortive complexes involve the same active site. The special conditions under which the Mb** site is occupied are those of optical pumping where the ligand positions involving a more rapid reaction are recombined (Mb*CO) while ligand positions involving a slower reaction are occupied. The X-ray absorption studies indentify a family of sites near the iron atom, and correlation with X-ray crystal structural data indicates only one such site in the heme pocket or crevice. The role of such a site in ligand binding can be viewed as a "facilitator" of ligand binding that guides the ligand into the active site. An appropriate trajectory to the active site is via the Mb** site which would afford orientation and alignment of the ligand for assuming a CO position from which binding would rapidly occur. In other words, the rotations and translations of the ligand that are permitted within the heme pocket are modulated by the Mb** binding site in such a way that the ligand is optimally oriented for further progress toward the active site. These geminate states may not only be functional but may also be keys to the reactivity of heme proteins with gaseous ligands.

In summary, these structural studies of trapped and pumped states of the ligand near the iron atom suggest that there are discrete way stations or "docking sites" on the ligand route to the heme that represent low-affinity binding sites on the reaction pathway (Chance et al., 1987). As such, these sites may alter the ligand pathway and modify barriers to recombination.

Registry No. Carbon monoxide, 630-08-0; iron, 7439-89-6; heme, 14875-96-8.

REFERENCES

Agmon, N., & Hopfield, J. J. (1983) *J. Chem. Phys. 78*, 6947.

Alben, J. O., Beece, D., Bowne, S. F., Doster, W., Eisenstein, L., Frauenfelder, H., Good, D., McDonald, J. C., Marden, M. C., Moh, P. P., Reinisch, L., Reynolds, A. G., Shyamsunder, E., & Yue, K. T. (1982) *Proc. Natl. Acad. Sci. U.S.A. 79*, 3744–3748.

Alberding, N., Austin, R., Beeson, K., Chan, S., Eisenstein, L., Frauenfelder, H., & Nordlund, T. (1976a) *Science (Washington, D.C.) 192*, 1002–1004.

Alberding, N., Austin, R. H., Chan, S. S., Eisenstein, L., Frauenfelder, H., Gunsalus, I. C., & Nordlund, T. M. (1976b) *J. Chem. Phys. 65*, 4701–4711.

Alberding, N., Chan, S., Eisenstein, L., Frauenfelder, H., Good, D., Gunsalus, I. C., Nordlund, T. M., Perutz, M. F., Reynolds, A. H., & Sorensen, L. B. (1978) *Biochemistry 17*, 43.

Ansari, A., Berendzen, J., Bowne, S. F., Frauenfelder, H., Iben, I. E. T. Sauke, T. B., Shyamsunder, E., & Young, R. D. (1985) *Proc. Natl. Acad. Sci. U.S.A. 82*, 5000–5004.

Austin, R. H., Beeson, K. W., Eisenstein, L., Frauenfelder, H., Gunsalus, I. C., & Marshall, V. P. (1973) *Science (Washington, D.C.) 181*, 541–543.

Austin, R. H., Beeson, K. W., Eisenstein, L., Frauenfelder, H., & Gunsalus, I. C. (1975) *Biochemistry 14*, 5355–5373.

Bray, R. C. (1964) in *Rapid Mixing and Sampling Techniques in Biochemistry* (Chance, B., Eisenhardt, R., Gibson, Q. H., & Lonberg-Holm, K. K., Eds.) pp 195–203, Academic, New York.

Campbell, B. F., & Friedman, J. M. (1987) *Biophys. J. 51*, 291a.

Chance, B., Graham, N., & Legallais, V. (1975) *Anal. Biochem. 67*, 552–579.

Chance, B., Schoener, B., Oshino, R., Itsak, F., & Nakase, Y. (1979) *J. Biol. Chem. 254*, 4764–4771.

Chance, B., Pennie, W., Carmen, M., Legallais, V., & Powers, L. (1982) *Anal. Biochem. 124*, 248–257.

Chance, B., Fischetti, R., & Powers, L. (1983) *Biochemistry 22*, 3820–3829.

Chance, B., Powers, L., Ching, Y., Poulos, T., Schonbaum, G. R., Yamazaki, I., & Paul, K.-G. (1984) *Arch. Biochem. Biophys. 235*, 596–611.

Chance, B., Korszun, K., Khalid, S., Alter, C., Sorge, J., & Gabbidon, E. (1986) in *Structural Biological Applications*

of X-ray Absorption, Scattering, and Diffraction (Bartunik, H. D., & Chance, B., Eds.) pp 49–71, Academic, New York.

Chance, B., Chance, M., Powers, L., Zhou, Y.-H., & Reddy, K. S. (1987) *Biophys. J. 51*, 460a.

Chance, M. (1986) Ph.D. Thesis, University of Pennsylvania, Philadelphia, PA.

Chance, M., Parkhurst, L., Powers, L., & Chance, B. (1986) *J. Biol. Chem. 261*, 5689–5692.

Collman, J. P., Brauman, J., Collins, T., Iverson, B., Lang, G., Pettman, R., Sessler, J., & Walters, M. (1983) *J. Am. Chem. Soc. 105*, 3038–3052.

Dasgupta, S., Spiro, T. G., Johnson, C. K., Dalickas, G. A., & Hochstrasser, R. M. (1985) *Biochemistry 24*, 5295–5297.

DeVault, D., & Chance, B. (1966) *Biophys. J. 6*, 825–847.

Diesenhofer, J., Ett, O., Miki, K., Humber, R., & Michel, H. (1985) *Nature (London) 318*, 618–624.

Fiamingo, F. G., & Alben, J. O. (1984) *Appl. Spectrosc. 39*, 116–123.

Fiamingo, F. G., & Alben, J. O. (1985) *Biochemistry 24*, 7964–7970.

Findsen, E. W., Scott, T., Friedman, J., Ondrias, M. R., & Chance, M. (1985) *J. Am. Chem. Soc. 107*, 3355–3359.

Frauenfelder, H. (1985) in *Structure and Motion: Membranes, Nucleic Acids and Proteins* (Clementi, E., Corongiu, G., Sarma, M. H., & Sarma, R. H., Eds.) pp 205–217, Adenine Press, Guilderland, NY.

Hartmann, H., Parak, F., Steigemann, W., Petsko, G., Ringe Ponzi, D., & Frauenfelder, H. (1982) *Proc. Natl. Acad. Sci. U.S.A. 79*, 4967–4971.

Iizuka, T., Yamamoto, H., Kotani, M., & Yonetani, T. (1974a) *Biochim. Biophys. Acta 351*, 182–295.

Iizuka, T., Yamamoto, H., Kotani, M., & Yonetani, T. (1974b) *Biochim. Biophys. Acta 371*, 126–139.

Jones, T. A. (1982) in *Computational Crystallography* (Sayer, D., Ed.) pp 3303–3317, Clarendon, Oxford.

Kuriyan, J. (1986) Ph.D. Thesis, Massachusetts Institute of Technology, Cambridge, MA.

Kuriyan, J., Wilz, S., Karplus, M., & Petsco, G. (1986) *J. Mol. Biol. 192*, 133–154.

Marcolin, H. E., Reschke, R., & Trautwein, A. (1979) *Eur. J. Biochem. 96*, 119–123.

Marden, M. (1982) *Eur. J. Biochem. 128*, 399–404.

Martin, J. L., Migus, A., Poyart, C., Lecarpentier, Y., Astier, R., & Antonetti, A. (1983) *Proc. Natl. Acad. Sci. U.S.A. 80*, 173–177.

Michaelis, L., & Menten, M. (1913) *Biochem. Z. 49*, 333–369.

Norwell, J., Numes, A., & Schoenborn, B. (1975) *Science (Washington, D.C.) 190*, 568–570.

Ogryzlo, E., & Porter, G. (1963) *J. Chem. Educ. 40*, 258–261.

Phillips, S. (1980) *J. Mol. Biol. 142*, 531–554.

Powers, L., Sessler, J. L., Woolery, G. L., & Chance, B. (1984) *Biochemistry 23*, 5519–5523.

Roder, H., Berendzen, J., Bowne, S., Frauenfelder, H., Sauke, T. B., Shyamsunder, E., & Weissman, M. B. (1984) *Proc. Natl. Acad. Sci. U.S.A. 81*, 2359–2363.

Rothgeb, T. M., & Gurd, F. R. W. (1978) *Methods Enzymol. 52*, 473–485.

Rousseau, D. L., & Argade, P. (1986) *Proc. Natl. Acad. Sci. U.S.A. 83*, 1310–1314.

Sassaroli, M., Dasgupta, S., & Rousseau, D. (1986) *J. Biol. Chem. 261*, 13704–13713.

Spartalian, K., Lang, G., & Yonetani, T. (1976) *Biochim. Biophys. Acta 428*, 281–290.

Yonetani, T., Iizuka, T., Yamamoto, H., & Chance, B. (1973) in *Oxidases and Related Redox Systems* (King, T. E., Mason, H. S., & Morrison, M., Eds.) Vol. 1, pp 401–405, University Park Press, Baltimore.